
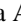
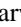




Efficient terahertz emission from R-plane α -Fe₂O₃/Pt

Rekha Agarwal ^{1,*}, Ziqi Li ^{2,*}, Kacho Imtiyaz Ali Khan ¹, Elbert E. M. Chia ^{2,†} and P. K. Muduli ^{1,‡}

¹*Department of Physics, Indian Institute of Technology Delhi, Hauz Khas, New Delhi-110016, India*

²*Division of Physics and Applied Physics, School of Physical and Mathematical Sciences, Nanyang Technological University, Singapore 637371, Singapore*



(Received 21 February 2024; revised 17 April 2024; accepted 15 May 2024; published 4 June 2024)

We report on the generation of ultrafast spin currents through femtosecond laser excitation of epitaxial bilayer thin films comprising α -Fe₂O₃ (an insulating antiferromagnet) and Pt (a heavy metal). The epitaxial thin films of α -Fe₂O₃ were simultaneously grown in three distinct orientations, namely, R, A, and C planes, employing pulsed laser deposition. By using the R plane α -Fe₂O₃, we demonstrate a substantial enhancement of the THz signal, nearly one order of magnitude greater compared to the A and C planes α -Fe₂O₃/Pt. We perform a detailed investigation into the sample azimuthal and laser polarization dependence of the THz emission. Our investigations establish that the sample azimuthal dependence of THz emission in the α -Fe₂O₃/Pt system is linked to the spin domain distribution as well as the crystalline symmetry of the orientation of α -Fe₂O₃. These results contribute significantly to understanding the ultrafast dynamics of spin currents in antiferromagnets.

DOI: [10.1103/PhysRevB.109.224408](https://doi.org/10.1103/PhysRevB.109.224408)

I. INTRODUCTION

Antiferromagnets (AFMs) have recently attracted significant attention for the development of the next generation of spintronic devices [1–4]. In an AFM, the two coupled sublattices with spontaneous magnetic moments in opposite directions create the net zero magnetic moment. This inherent property provides notable advantages, such as the lack of stray fields and remarkable stability to external magnetic fields. These qualities make AFMs promising for high-density spintronic memory applications [5]. Another remarkable advantage of AFMs is their extremely high intrinsic frequency (THz) of antiferromagnetic dynamics, offering the potential to elevate the processing speed of memory elements from gigahertz to terahertz regimes [1,6].

Another emerging phenomenon of antiferromagnetic materials in spintronics involves the generation of terahertz (THz) emission by using laser-induced ultrafast spin current. Such a process of spintronic-based THz emission was first discovered in ferromagnet/heavy metal heterostructures [7–9]. In such structures, an ultrafast spin current generated in the ferromagnet is converted into charge current through the inverse spin Hall effect in the heavy metal layer. The resulting ultrafast transient charge current emits electromagnetic radiation in the THz frequency range [10–15]. Recently, this phenomenon was observed in antiferromagnetic/heavy metal heterostructures [16–19]. While it was first observed in NiO/Pt [16], it has also been recently demonstrated in α -Fe₂O₃/Pt [18].

Similar to NiO, α -Fe₂O₃ or hematite is also an insulating antiferromagnet at room temperature. α -Fe₂O₃ is antifer-

romagnetic between the Morin transition temperature of ≈ 260 K [20,21] and Néel temperature of 950 K. Furthermore, α -Fe₂O₃ possesses a low Gilbert damping constant and a large spin diffusion length [22–25]. Recently, the spin pumping from the acoustic resonant mode in α -Fe₂O₃ was also reported [26]. These reports indicated that α -Fe₂O₃ is a highly promising material for various spintronics-based devices [21,27–30].

The recent study of THz emission on α -Fe₂O₃/Pt was performed on (0001)-oriented α -Fe₂O₃ films grown on C plane Al₂O₃ substrate. [18] To date, no studies of THz emission have been performed on other orientations of α -Fe₂O₃ films. Previous studies have indicated that the R plane of α -Fe₂O₃ is highly promising for efficient generation of spin-orbit torque [31] as well as for long-range spin transport [23]. Consequently, investigating THz emission in other low-index directions, specifically the A and R plane α -Fe₂O₃, is particularly interesting.

In this work, we report on zero field THz emission from α -Fe₂O₃/Pt thin films for three distinct orientations of α -Fe₂O₃, namely, the C plane, A plane, and R plane. First, we demonstrate the growth of high-quality epitaxial thin films of the C plane, A plane, and R plane α -Fe₂O₃ on the sapphire substrate. Then, we systematically studied THz emission from α -Fe₂O₃/Pt having different orientations as a function of sample azimuth and laser polarization. We find a substantial enhancement of the THz signal in the R-plane α -Fe₂O₃, nearly one order of magnitude greater compared to the C plane and A plane α -Fe₂O₃/Pt. We show that the symmetry of the sample azimuthal dependence of THz emission in our α -Fe₂O₃/Pt system is related to the spin domain distribution, as well as the crystalline symmetry.

α -Fe₂O₃ has a rhombohedral corundum crystal structure with Fe⁺³ ions on the basal plane with AFM coupling between adjacent planes. The atomic arrangement in the basal plane is hexagonal due to which several studies have shown epitaxial

*These authors contributed equally to this work.

†ElbertChia@ntu.edu.sg

‡muduli@physics.iitd.ac.in

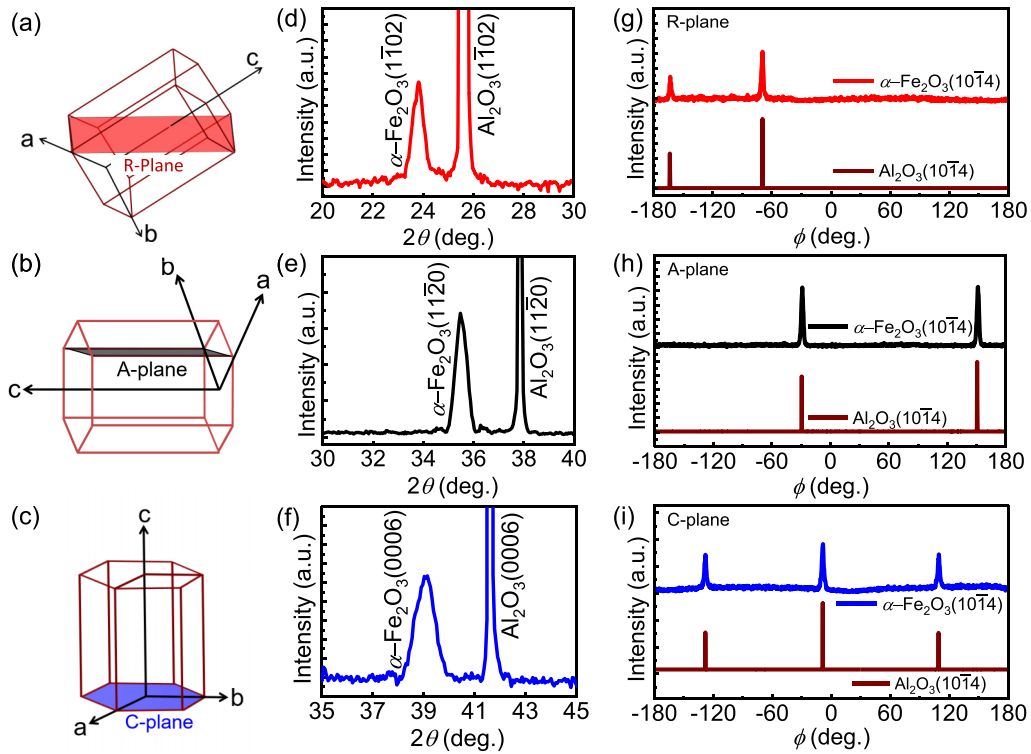


FIG. 1. Unit cell of α -Fe₂O₃ showing (a) R plane, (b) A plane, and (c) C plane. The XRD θ - 2θ scan of (d) R plane, (e) A plane, and (f) C plane α -Fe₂O₃ thin films. The ϕ scan data of (10 $\bar{1}$ 4) reflection of both α -Fe₂O₃ and Al₂O₃ for (g) R pane, (h) A plane, and (i) C plane. For clarity, different intensity scales are utilized for Al₂O₃ and α -Fe₂O₃ in figures (g)–(i).

growth of α -Fe₂O₃ on hexagonal Al₂O₃ [32,33] despite the lattice mismatch of 5.8% between Al₂O₃ and α -Fe₂O₃. We employ the pulsed laser deposition method to *simultaneously* grow epitaxial thin films of α -Fe₂O₃ on (0001)-oriented (C plane), (11 $\bar{2}$ 0)-oriented (A plane), and (1 $\bar{1}$ 02)-oriented (R plane) Al₂O₃ substrates, respectively. The three orientations of the α -Fe₂O₃ are shown schematically in Figs. 1(a) to 1(c).

II. EXPERIMENTAL DETAILS

KrF excimer pulsed laser source with a wavelength of 248 nm, laser energy density of 1.1 J/cm², and a repetition rate of 10 Hz is employed for the deposition of α -Fe₂O₃ thin films. The substrate-to-target distance was set at 5.6 cm throughout the deposition and the Fe₂O₃ target was rotated continuously at 5 rpm for uniform growth. We find the growth rate of α -Fe₂O₃ thin films to be 0.028 Å per laser shot. The base pressure of the chamber was better than 2×10^{-6} Torr. During the deposition, oxygen partial pressure of 3.75×10^{-3} Torr was maintained. The best quality of films was obtained for the substrate temperature of 550 °C. After the growth of α -Fe₂O₃, the sample was moved to a different ultrahigh vacuum (AJA Orion 8) sputtering system to grow the Pt layer. The base pressure of the sputtering chamber was better than 4×10^{-8} Torr. The α -Fe₂O₃ film was exposed to air during the sample transfer from the pulsed laser deposition system to the sputtering system. Therefore, before the Pt layer deposition, the α -Fe₂O₃ film surface was cleaned by removing 3 nm- α -Fe₂O₃ (at etch rate of 0.125 Å/s) using RF substrate bias.

Subsequently, a 3-nm-thick Pt layer was deposited at room temperature with a working pressure of 2×10^{-3} Torr. The growth rate of the Pt layer was 0.4 Å/s.

High-resolution x-ray diffraction (HRXRD) was employed to characterize the crystallographic properties of α -Fe₂O₃ thin films. The epitaxial relationship of α -Fe₂O₃ was determined through ϕ -scan analysis. The film thicknesses were determined using x-ray reflectivity (XRR). These measurements were performed using a PANalytical x-ray diffractometer, utilizing Cu-K α radiation with a wavelength of 1.54 Å. The Raman measurement was performed using a Renishaw inVia confocal microscope with a 532-nm-laser wavelength and 2400 lines per mm grating at 10-mW power. We conducted THz emission measurements on α -Fe₂O₃/Pt samples using a time-domain THz spectroscopy experimental setup [34]. The samples were excited by a femtosecond laser at normal incidence. Optical excitation was achieved using the output from a Ti:sapphire regenerative amplifier, providing approximately 35 femtosecond pulses at a 1-kHz repetition rate and centered around 800 nm. The laser output was split into two parts using a beam splitter, with a stronger portion serving as the optical pump for excitation and a weaker portion as the probe for detecting the THz pulses. A pair of parabolic mirrors directed the emitted THz radiation to a 1-mm-thick [110]-oriented ZnTe nonlinear crystal, which was utilized for detecting the THz pulses. All the measurements are performed without any magnetic field. THz-pulse detection employed the electro-optic sampling technique, where the probe beam was collinearly overlapped with THz pulses on the ZnTe crystal. A computer-controlled linear translational stage controlled the

delay between them. The THz pulse-induced birefringence in the probe was detected using a balanced photodetector, lock-in amplifier, quarter-wave plate, and Wollaston prism. The differential signal obtained was directly proportional to the THz electric field. All measurements were conducted under ambient conditions of temperature and humidity.

III. RESULTS AND DISCUSSION

Figures 1(d) to 1(f) illustrates the HRXRD θ - 2θ scan for 20-nm-thick R, A, and C planes α -Fe₂O₃ thin films. On the R-plane Al₂O₃ substrate, Bragg peaks corresponding to the reflection from (1 $\bar{1}$ 02)-planes of Fe₂O₃ were observed at 23.75°, as depicted in Fig. 1(d). When grown on the A-plane Al₂O₃ substrate, the Fe₂O₃(11 $\bar{2}$ 0) reflection was positioned at 35.27°, as shown in Fig. 1(e). On the C-plane Al₂O₃ substrate, Bragg peaks corresponding to the reflection from (0006) planes of Fe₂O₃ was observed at 38.93°, as illustrated in Fig. 1(f). The long-range HRXRD θ - 2θ scan is shown in the Appendix information (Appendix A). The absence of other peaks indicates the epitaxial growth of the Fe₂O₃ film on C-, A-, and R-plane Al₂O₃ substrates.

To further confirm the epitaxial relationship, we performed ϕ scan measurements. We used (10 $\bar{1}$ 4) reflection of Al₂O₃ ($2\theta = 35.148^\circ$) and α -Fe₂O₃ ($2\theta = 33.15^\circ$) for all three cases R, A, and C planes α -Fe₂O₃. The sample surface was tilted by an angle, χ for the (10 $\bar{1}$ 4) reflection, which was 47°, 57.56°, and 38.2° for the case of R, A, and C planes, respectively. In the case of R-plane α -Fe₂O₃ thin films, the ϕ scan exhibits two peaks with a 90° interval were observed for both the substrate Al₂O₃ and α -Fe₂O₃ as depicted in Fig. 1(g). In the case of A-plane α -Fe₂O₃ thin film, the ϕ scan exhibits two peaks with a 180° interval for both the substrate Al₂O₃ and the thin film α -Fe₂O₃ as depicted in Fig. 1(h). Finally in the case of C-plane α -Fe₂O₃ thin film, the ϕ scan exhibits three peaks with a 120° interval for both the substrate Al₂O₃ and the thin film α -Fe₂O₃ as depicted in Fig. 1(i). These results indicate that the in-plane directions of α -Fe₂O₃ and Al₂O₃ are parallel to each other without any twinning or rotation, which is similar to previous studies [32,35].

Raman measurements were employed to confirm further the crystalline quality and phase of the grown α -Fe₂O₃ thin films. Figure 2 presents the Raman measurement for 20-nm-thick R, A, and C planes α -Fe₂O₃ films. Seven phonon modes, including $5E_g$ and $2A_g$, were observed, corresponding to 247, 294, 379, 416, and 573 cm⁻¹ for $5E_g$ modes and 226 and 495 cm⁻¹ for $2A_g$ modes, respectively. These findings confirm the corundum structure of the grown α -Fe₂O₃ thin film [36–38]. The presence of an infrared (IR) active mode around 665 cm⁻¹ in all the three orientations of α -Fe₂O₃ indicates the presence of disorder in the film. This peak is normally observed in thin films of α -Fe₂O₃. [39] The mode observed around 740 cm⁻¹ arises from the Al₂O₃ substrate [40]. A weak and broad vibrational mode at around 834 cm⁻¹ is assigned to a magnon excitation [39], confirming the antiferromagnetic nature of α -Fe₂O₃ films. The signature of weak two-magnon mode at around 1550 cm⁻¹ is also observed. Finally, a broad peak around 1320 cm⁻¹ is assigned to the $2E_u$ (LO) mode, which originates from two-phonon scattering and is known to be resonantly enhanced [39]. We also observe

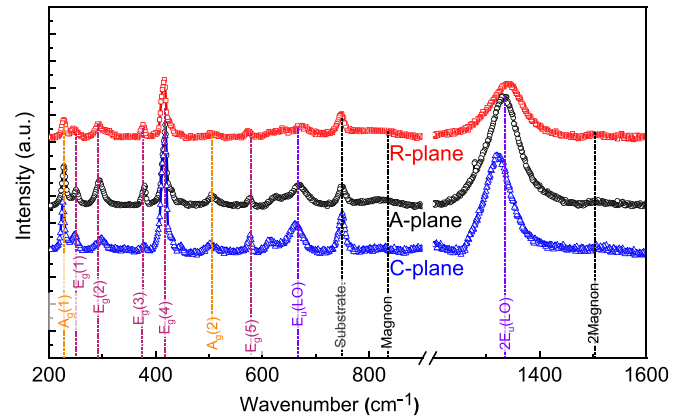


FIG. 2. Raman spectra obtained using 532-nm-laser excitation of α -Fe₂O₃/Pt heterostructure grown in R, A, and C planes.

a small shift of the $2E_u$ (LO) mode in the C-plane sample towards the lower wave number, which is likely due to the stretching of the Fe-O bond, as previously reported in Fe₂O₃ by using combined Raman and x-ray absorption near-edge structure measurements [36]. The bond stretching in the C plane may be due to a slightly different state of strain compared to other orientations.

The surface roughness and morphology were determined by atomic force microscopy (AFM), which are shown in Appendix A. The surface roughness of the α -Fe₂O₃ films with R, A, and C planes are comparable (<0.4 nm), which is expected as the films are grown under identical conditions. The magnetization measurements performed on R, A, and C planes α -Fe₂O₃ films were found to be dominated by the diamagnetic contribution of the substrate with no noticeable difference in magnetization for the three orientations as shown in Appendix B. The behavior is consistent with the antiferromagnetic nature of the α -Fe₂O₃ films.

Figure 3(b) shows the example of the detected THz emission signal performed on the R, A, and C planes α -Fe₂O₃/Pt heterostructure. The coordinate system (xyz) is defined in the laboratory frame as shown in Fig. 3(a). The laser light is incident along the y -axis. For the linear polarization of the laser, the polarization direction, θ_p , is defined w.r.t the x -axis. The sample azimuth, θ_s is also defined w.r.t the x -axis. The THz emission spectra in Fig. 3 are recorded at θ_s , which shows maximum THz amplitude for $\theta_p = 0^\circ$. The amplitude of the THz emission signal is found to depend strongly on the orientation of α -Fe₂O₃ thin films. The THz signal in the R-plane α -Fe₂O₃/Pt system exhibits an order of magnitude higher amplitude compared to the C- and A-plane α -Fe₂O₃/Pt. A comparison of the amplitude with the reference Fe/Pt is shown in the Appendix C. The fast Fourier transformation (FFT) of these signals is shown in the inset of Fig. 3, which shows that the bandwidth of generated THz emission is similar (~ 2 THz) for all three cases. Note that our measurement setup bandwidth is about 3 THz. Measurements done on the bare α -Fe₂O₃ do not show any THz signals, as shown in the Appendix D. Hence, the THz signal originates primarily from the bilayer α -Fe₂O₃/Pt via the spin-to-charge conversion (SCC), which is similar to the recent report by Qiu *et al.* [18].

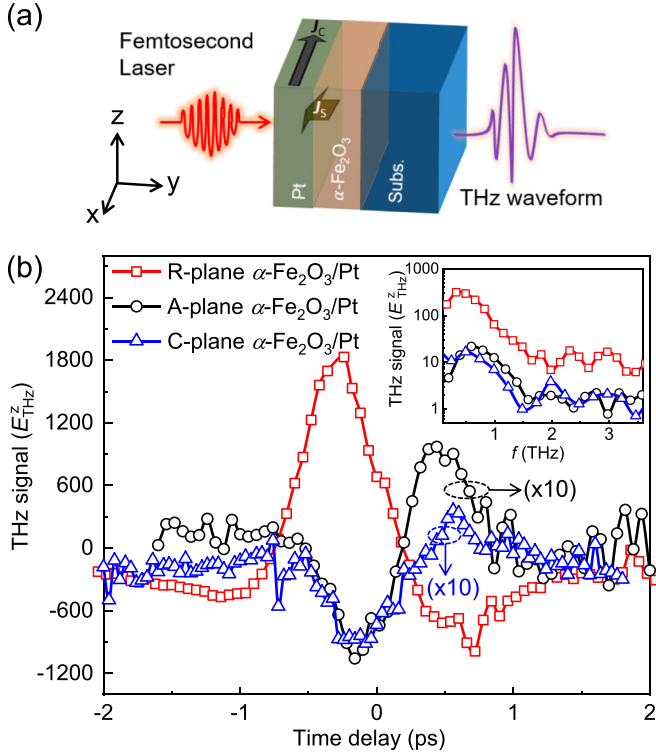


FIG. 3. (a) Schematic of the transmission-type THz spectroscopy setup. The xyz coordinate system is defined in the laboratory's frame. The sample is placed in the xz plane, while the laser is incident along the y -direction. (b) THz signal, E_{THz}^z from R, A, and C planes $\alpha\text{-Fe}_2\text{O}_3/\text{Pt}$ heterostructure grown on Al_2O_3 substrates. The inset displays the corresponding Fourier spectra of the THz signal.

To understand the origin of THz generation in $\alpha\text{-Fe}_2\text{O}_3/\text{Pt}$ system, we performed a detailed study of THz emission as a function of sample azimuth (first column) and laser polarization (second column) as shown in Fig. 4. The sample azimuthal-dependent THz emission measurements are taken for $\theta_p = 0^\circ$. In the R-plane $\alpha\text{-Fe}_2\text{O}_3/\text{Pt}$, the sample azimuthal dependence of THz amplitude displays one-fold symmetry [Fig. 4(a)], while the corresponding XRD ϕ -scan data [Fig. 1(g)] exhibits a two-fold symmetry. Consequently, factors other than crystal symmetry influence the sample azimuthal dependence of the THz amplitude for the R-plane $\alpha\text{-Fe}_2\text{O}_3/\text{Pt}$. However, in the A-plane $\alpha\text{-Fe}_2\text{O}_3/\text{Pt}$, the azimuthal dependence of THz amplitude exhibits two-fold symmetry [Fig. 4(b)], which is consistent with the XRD ϕ -scan data [Fig. 1(h)], which also exhibits a two-fold symmetry. Finally, for the C-plane $\alpha\text{-Fe}_2\text{O}_3/\text{Pt}$, the sample azimuthal dependence of THz amplitude displays one-fold symmetry [Fig. 4(c)], while the corresponding XRD ϕ -scan data [Fig. 1(i)] exhibits a three-fold symmetry. Hence, factors other than crystal symmetry are also found to influence the sample azimuthal dependence of the THz amplitude for the C-plane $\alpha\text{-Fe}_2\text{O}_3/\text{Pt}$. This result appears to contradict the results of Qiu *et al.* [18], which was performed only for the C-plane $\alpha\text{-Fe}_2\text{O}_3/\text{Pt}$. The sample azimuthal dependence of THz amplitude in the work by Qiu *et al.* exhibited three-fold symmetry, in agreement with the crystal symmetry of C-plane $\alpha\text{-Fe}_2\text{O}_3$.

The second column of Fig. 4 shows the behavior of THz amplitude with laser polarization angle, θ_p . For the R-plane $\alpha\text{-Fe}_2\text{O}_3$ the measurement is performed at $\theta_s = 0^\circ$ [Fig. 4(d)]. However, for A- and C-planes $\alpha\text{-Fe}_2\text{O}_3/\text{Pt}$, these measurements are performed for $\theta_s = 180^\circ$, and 270° , respectively [Figs. 4(e) and 4(f)]. These values of θ_s were chosen to maximize the signal to noise as the THz amplitude was found to be very weak for A- and C-planes $\alpha\text{-Fe}_2\text{O}_3/\text{Pt}$ thin films. The THz signal can be effectively fitted with $P_0 + P_1 \cos 2(\theta_p)$ terms for all three orientations. In the case of R- and A-planes $\alpha\text{-Fe}_2\text{O}_3/\text{Pt}$ the polarization modulation (P_1/P_0) of THz amplitude is about 10%, whereas it is about 30% for the C-plane $\alpha\text{-Fe}_2\text{O}_3/\text{Pt}$. The tunability of THz amplitude in the $\alpha\text{-Fe}_2\text{O}_3/\text{Pt}$ heterostructure with pump polarization differs from spintronic THz emitter based on ferromagnets and heavy metal [7–9], but is similar to that of AFM/HM systems such as NiO/Pt [16,17,41] and $\alpha\text{-Fe}_2\text{O}_3/\text{Pt}$ [18].

Now, we will discuss the mechanism of orientation-dependent THz emission in $\alpha\text{-Fe}_2\text{O}_3/\text{Pt}$ system. In the case of AFM/HM system, the ultrafast spin current can be produced through both incoherent and coherent mechanisms. The incoherent mechanism includes the pyrospintronic effect (PSE) [7,42,43] and ultrafast spin Seebeck effect (SSE) [8,42,44], while the coherent mechanism includes impulsive stimulated Raman scattering (ISRS). In the incoherent processes, PSE and SSE, the ultrafast spin current is produced by heating-induced spin-voltage and a temperature gradient across the AFM/HM interface, respectively. These methods require a nonzero net magnetization within the magnetic layer. In our case, all the measurements are performed at zero magnetic field. We also did not observe any significant difference in the magnetization of R-, A-, and C-planes $\alpha\text{-Fe}_2\text{O}_3/\text{Pt}$, which can explain the observed difference in THz peak amplitude for the three orientations. Hence, we neglect the incoherent driving forces as a possible mechanism to explain the observed behavior.

On the other hand, the coherent ISRS mechanism does not require a nonzero net magnetization and has been applied to explain the THz emission from both NiO/Pt [16] and $\alpha\text{-Fe}_2\text{O}_3/\text{Pt}$ [18] systems. The ISRS process induces an impulsive magnetization $\Delta M(t)$ in the $\alpha\text{-Fe}_2\text{O}_3$ layer, which produces an ultrafast antiferromagnetic spin pumping to the adjacent Pt layer. Consequently, the injected ultrafast spin current in the Pt layer is converted to THz pulses via the inverse spin Hall effect. A signature of the ISRS process [45,46] is the dependence of THz amplitude on the laser polarization, which we observe in Fig. 4. The THz emission in our geometry due to the ISRS origin can be phenomenologically described as [16]

$$E_{\text{THz}}^z \propto A_0 + A_1 \cos(\theta_s - \delta) + A_2 \cos(2\theta_s - \delta), \quad (1)$$

where coefficients A_0 , A_1 , and A_2 are functions of nonlinear susceptibility tensor, $\chi_{i'j'k'}^{(2)\text{MEE}}$ and a ratio η_n , which represents the contribution from the n^{th} domain. The nonlinear susceptibility tensor $\chi_{i'j'k'}^{(2)\text{MEE}}$ describes the relationship between AC magnetization and the laser electric field, which is parametrically generated by simulated Raman-type nonlinear process [16,47–49]. Here, $i'j'k'$ refers to the spin coordinate system of the $\alpha\text{-Fe}_2\text{O}_3$ lattice. We assume that our samples consist of

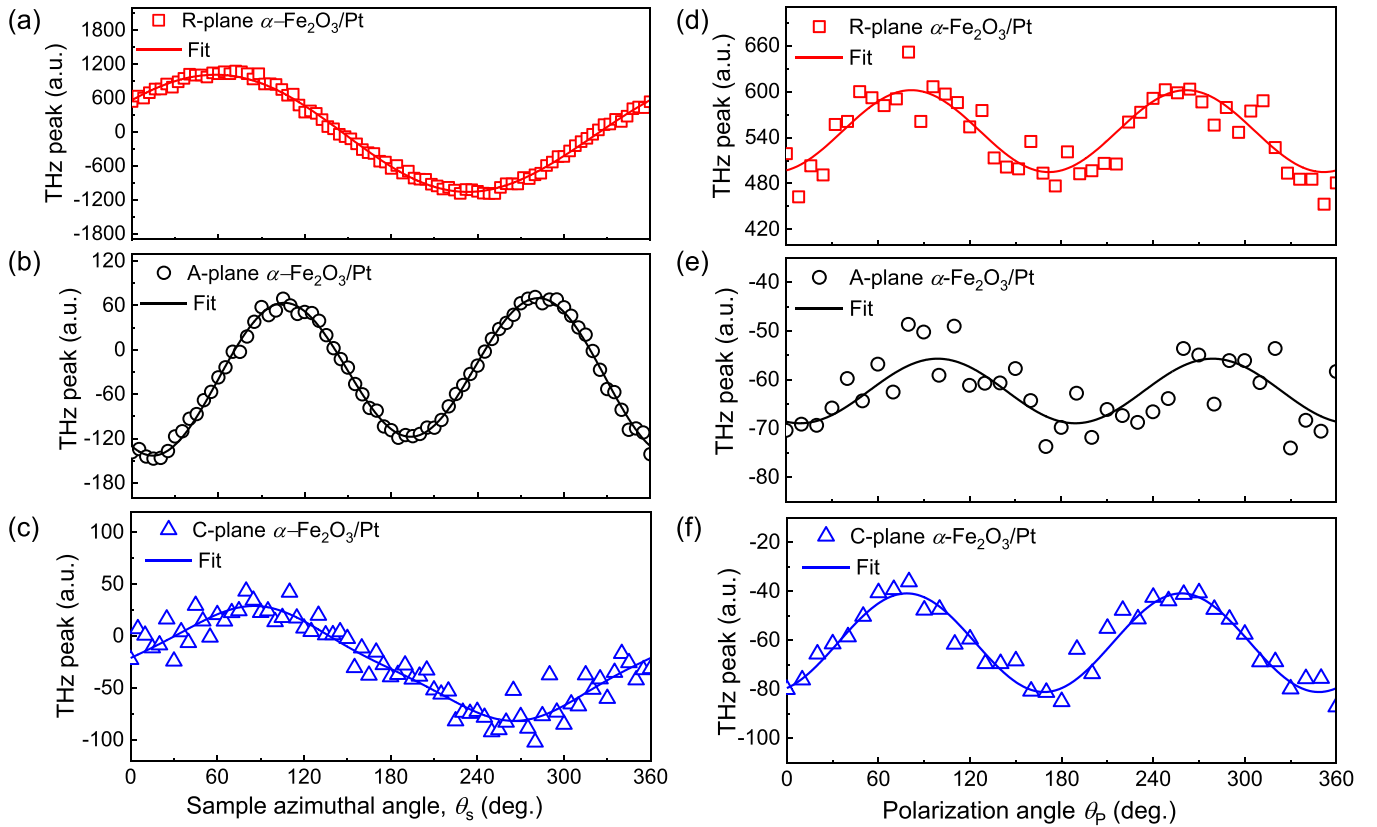


FIG. 4. Sample azimuthal angle (θ_s) dependent THz emission in α -Fe₂O₃ heterostructures in three different orientations: (a) R-plane α -Fe₂O₃/Pt, where $\theta_s = 0^\circ$ corresponds to the $[1\bar{1}00]$ axis of the R plane of the Al₂O₃ substrate; (b) A plane α -Fe₂O₃/Pt, where $\theta_s = 0^\circ$ corresponds to the $[0001]$ axis of the A plane of the Al₂O₃ substrate; (c) C plane α -Fe₂O₃/Pt, where $\theta_s = 0^\circ$ corresponds to the $[1\bar{1}00]$ axis of the C plane of the Al₂O₃ substrate. Polarization angle (θ_p) dependent THz emission in thin film of (d) R-plane α -Fe₂O₃/Pt at constant $\theta_s = 0^\circ$, (e) A-plane α -Fe₂O₃/Pt at constant $\theta_s = 180^\circ$, and (f) C-plane α -Fe₂O₃/Pt at constant $\theta_s = 270^\circ$.

randomly distributed domains. The domain sizes of α -Fe₂O₃ are typically of the order of 1 μ m, [50] which is significantly smaller than the size of the laser spot, which is about 1.5 mm. Finally, the angle δ accommodates offset arising from the experimental setup. We fit the sample azimuthal dependence with the above equation as shown by the solid lines in Fig. 4. The term A_1 (one-fold) are found to be the most dominant term for R and C planes, while both the terms A_1 (one-fold) and A_2 (two-fold) are found essential for the fitting of sample azimuthal dependence of THz peak for A-plane α -Fe₂O₃/Pt. Furthermore, the value of A_1 is found to be 1035 ± 4 for the R plane, which is about 20 times higher than that of the C-plane ($A_1 = -52 \pm 2$).

To explain this behavior, we invoke the crystalline and magnetic symmetry. According to Eq. (1), the amplitude of THz emission depends on the summation of spin currents generated in each magnetic domain via the ISRS mechanism. Hence, the distribution of spin domains can significantly influence both the amplitude and the sample azimuthal dependence of THz emission. In α -Fe₂O₃, the easy axes are along all (1100) axes, which changes the three-fold crystalline symmetry of the C plane and R plane, while it does not affect the two-fold symmetry of A-plane α -Fe₂O₃. [18] This explains why the sample azimuthal dependence of THz peak for A-plane α -Fe₂O₃/Pt still exhibits the two-fold symmetry consistent with the XRD ϕ -scan data [Fig. 1(h)]. The spin do-

main distribution in the C-plane and R-plane α -Fe₂O₃ changes the symmetry of the sample azimuthal dependence of THz emission. Qiu *et al.* [18] showed a three-fold symmetry of the sample azimuthal dependence of THz emission in the C plane, while we observed a one-fold symmetry. We attribute this difference to different spin domain distributions in our samples.

Finally, we discuss the possible origin of the large THz emission observed in R-plane α -Fe₂O₃/Pt. We believe the mechanism is related to a more efficient generation of ultrafast spin current by laser-induced transient magnetization. The ISRS process involves impulsive magnetization $\Delta M(t)$ in the α -Fe₂O₃ layer, giving spin pumping on a sub-picosecond time scale. Recent studies have shown that spin-orbit torque is more efficient in switching the Néel vector in R-plane α -Fe₂O₃/Pt for which the easy plane is tilted [31]. The R-plane α -Fe₂O₃ has a tilt angle of about 58° with the easy plane (C plane). Hence, the laser-induced effective fields can have components in the easy plane containing two sublattice magnetic moments m_A and m_B . This can rotate the two sublattices more constructively, leading to the highly efficient spin current generation in R-plane α -Fe₂O₃. Antiferromagnetic spin pumping experiments as a function of orientation of α -Fe₂O₃ such as those used by Vaidya *et al.* [51] and Li *et al.* [52], as well as spin-torque-driven antiferromagnetic resonance experiments reported recently by Zhou *et al.* [53] can help to confirm our hypothesis.

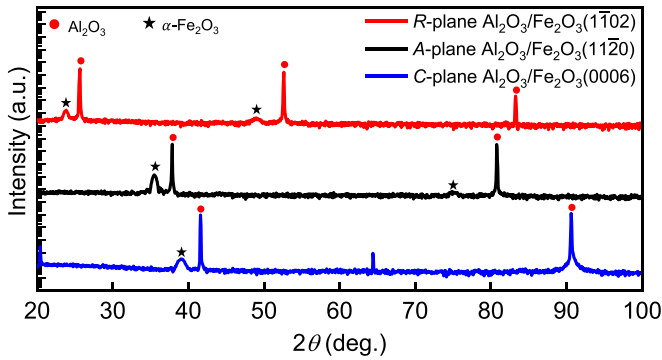


FIG. 5. Long range θ - 2θ x-ray diffraction scan of R, A, and C plane α - Fe_2O_3 thin films grown on R-, A-, and C-plane Al_2O_3 substrates, respectively. The black star and red dot are used to indicate the Bragg peaks corresponds to α - Fe_2O_3 film and Al_2O_3 substrate, respectively.

We note that laser-induced terahertz emission in antiferromagnetic/nonmagnetic structures is an emerging phenomenon. To fully understand the mechanism of the efficient THz emission from the R-plane α - $\text{Fe}_2\text{O}_3/\text{Pt}$ system, more comprehensive theoretical studies, particularly as a function of the orientation of α - Fe_2O_3 , are necessary. In this regard, theoretical studies similar to the recent work on off-resonant THz spin pumping by Sun *et al.* [54] could be beneficial.

IV. CONCLUSION

In conclusion, we demonstrated that THz amplitude and polarity can be tuned by adjusting the sample azimuthal orientation and the orientation of α - Fe_2O_3 thin films without needing an external magnetic field. We show an order of magnitude improvement in THz emission from epitaxial thin films of R-plane α - $\text{Fe}_2\text{O}_3/\text{Pt}$ as compared to the identical films grown with C- and A-plane orientations. Furthermore, we show that the orientation of α - Fe_2O_3 films also affects the symmetry of sample azimuthal dependence of THz peak amplitude, which is determined by both crystalline symmetry and magnetic symmetry of the orientations. Our work shows that the R-plane α - Fe_2O_3 is highly promising for THz spintronics. The results obtained from this study are highly promising and have tremendous potential for the advancement of spintronics-

based THz devices as well as the field of antiferromagnetic spintronics.

ACKNOWLEDGMENTS

The partial support from the Ministry of Human Resource Development under the IMPRINT program (Grants No. 7519 and No. 7058), the Department of Electronics and Information Technology (DeitY), the Science and Engineering Research Board (SERB File No. CRG/2018/001012 and No. CRG/2022/002821), Joint Advanced Technology Centre at IIT Delhi, Grand Challenge Project, IIT Delhi, and the Department of Science and Technology under the Nanomission program [Grant No. SR/NM/NT-1041/2016(G)] are gratefully acknowledged. We also acknowledge the Central Research Facility, IIT Delhi, for characterization facilities and the Department of Physics, IIT Delhi, for the pulsed laser deposition system. This work was supported by the Singapore Ministry of Education AcRF Tier 3 Programme “Geometrical Quantum Materials” (Grant No. MOE2018-T3-1-002), and AcRF Tier 2 “Dynamical characterization of the spin-to-charge conversion mechanisms in 2D heterostructures” (Grant No. MOE-T2EP50222-0014). R.A. acknowledges support from the Council of Scientific and Industrial Research (CSIR), India and India Connect @ NTU Visiting Research Student Programme. We also thank Dr. Sunil Kumar and Ms. Ekta Yadav for some test measurements and useful discussion.

APPENDIX A: STRUCTURAL CHARACTERIZATION OF α - $\text{Fe}_2\text{O}_3/\text{Pt}$ HETEROSTRUCTURE

1. X-ray diffraction

Figure 5 illustrates the long-range XRD θ - 2θ scan for the 20-nm-thick R-, A-, and C-planes α - Fe_2O_3 thin films. On the R-plane Al_2O_3 substrate, Bragg peaks corresponding to the reflection from $(1\bar{1}02)$ and $(2\bar{2}04)$ planes of α - Fe_2O_3 were observed at 23.75° and 48.94° , respectively. When grown on the A-plane Al_2O_3 substrate, the $\text{Fe}_2\text{O}_3(11\bar{2}0)$ reflection and $(22\bar{4}0)$ reflection were observed at 35.27° and 75.03° , respectively. On the C-plane Al_2O_3 substrate, Bragg peaks corresponding to the reflection from (0006) and (0012) planes of Fe_2O_3 were observed at 38.93° and 83.87° , respectively. The absence of peaks from other orientations indicates the

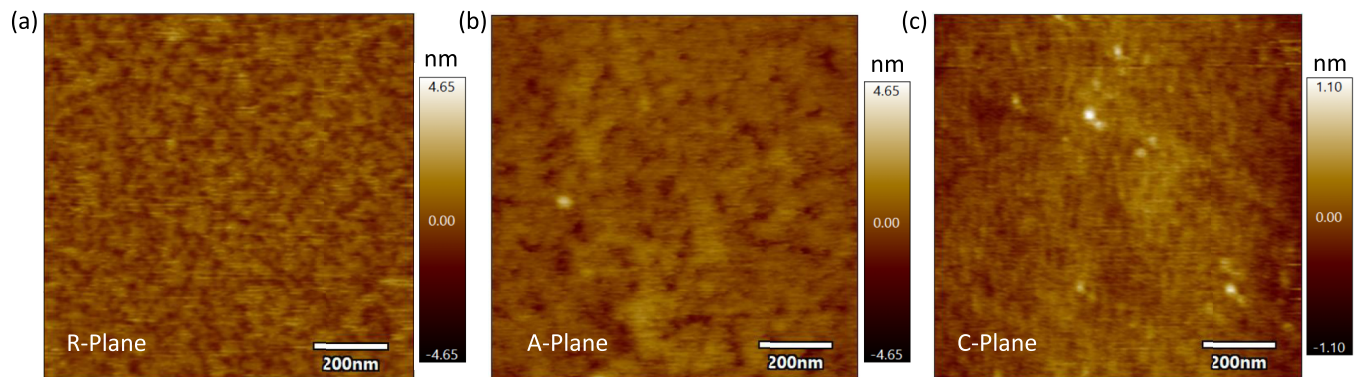


FIG. 6. Atomic force microscopy images of (a) R-, (b) A-, and (c) C-plane-oriented α - Fe_2O_3 thin films.

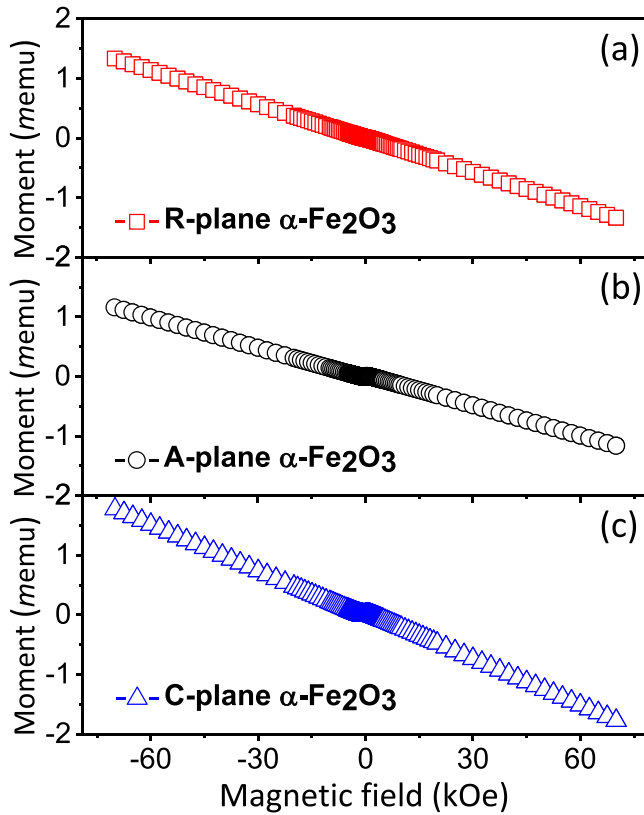


FIG. 7. Magnetization measurement in thin film of $\alpha\text{-Fe}_2\text{O}_3$ grown in (a) R-, (b) A-, and (c) C-plane orientation using quantum design PPMS system.

epitaxial growth of the Fe_2O_3 film on R-, A-, and C-plane Al_2O_3 substrates.

2. Atomic force microscopy

Figure 6 represents the topography of $\alpha\text{-Fe}_2\text{O}_3$ thin films with a scan area of $1\ \mu\text{m} \times 1\ \mu\text{m}$. All the measurements were performed at room temperature in tapping mode using Asylum research, MFP-3D system. The value of root-mean-square (rms) roughness of R-, A-, and C-plane $\alpha\text{-Fe}_2\text{O}_3$ films were found to be 0.36 nm, 0.34 nm, and 0.11 nm, respectively. The value of rms roughness for all the films is less than 0.4 nm, indicating smoother films surface, which is consistent with the previous reports on $\alpha\text{-Fe}_2\text{O}_3$ [18]. Overall, there is no major difference in surface roughness for the three different orientations of $\alpha\text{-Fe}_2\text{O}_3$ thin films.

APPENDIX B: MAGNETIC CHARACTERIZATION OF $\alpha\text{-Fe}_2\text{O}_3$ THIN FILM

The in-plane magnetization curves were obtained at room temperature using the magnetic property measurement system (MPMS) with a superconducting quantum interference device (SQUID). Figure 7, the magnetic moment was plotted as a function of external magnetic field (by sweeping the magnetic field from 70 kOe to -70 kOe) for the (a) R-, (b) A-, and (c) C-plane $\alpha\text{-Fe}_2\text{O}_3$ thin films. For all three cases, we observed a dominating diamagnetic contribution arising from their respective R-, A-, and C-planes Al_2O_3 substrate. However, a

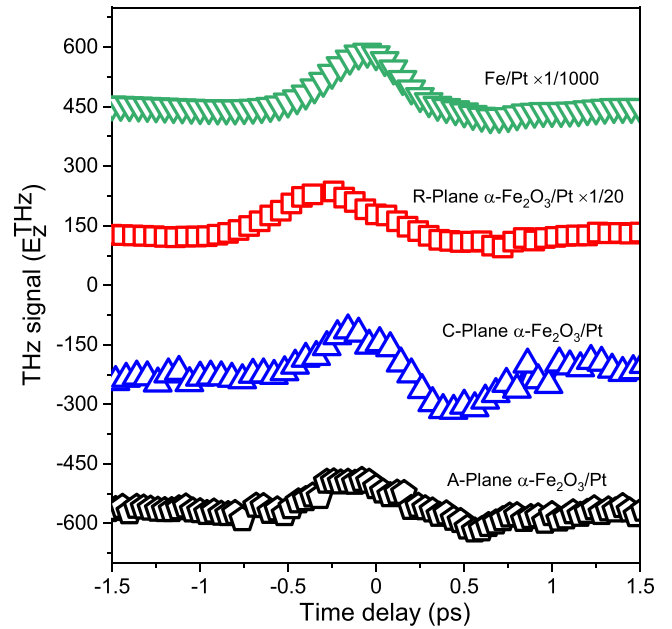


FIG. 8. Comparison of THz signal amplitude of R-, A-, and C-plane oriented $\alpha\text{-Fe}_2\text{O}_3/\text{Pt}$ heterostructure with the reference Fe/Pt sample. The THz amplitudes are shifted vertically for clarity.

weak “ferromagnetic-like” signal were observed for the all films in the low field region, which might be due to the flux-pinning of the superconducting solenoid. We also measure the magnetization curve for pristine Al_2O_3 substrate without films and observe a small ferromagnetic signal, indicating the “ferromagnetic-like” signal was not originated from the film.

APPENDIX C: COMPARISON OF THZ SIGNAL AMPLITUDE OF $\alpha\text{-Fe}_2\text{O}_3/\text{Pt}$ WITH REF Fe/Pt

We compared the THz amplitude of the R-, A-, and C-plane oriented $\alpha\text{-Fe}_2\text{O}_3/\text{Pt}$ heterostructures with a Fe/Pt sample, which is our reference sample. The results are presented

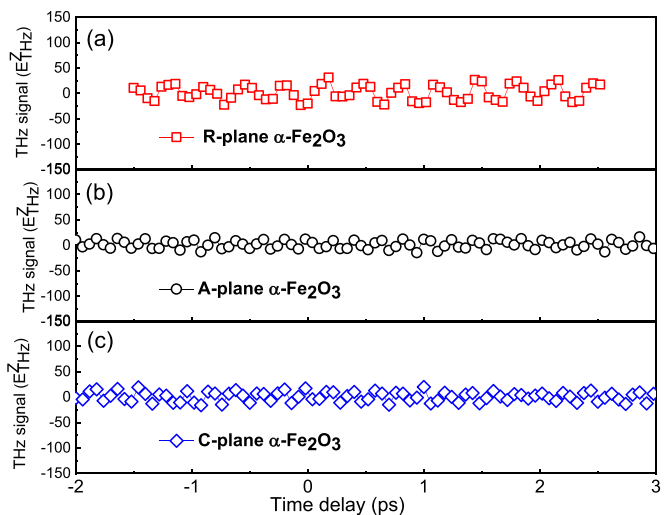


FIG. 9. THz measurement of only $\alpha\text{-Fe}_2\text{O}_3$ thin film grown in (a) R-, (b) A-, and (c) C-plane orientation.

in Fig. 8. We used identical setup conditions for all measurements. The THz amplitude of our C-plane α -Fe₂O₃/Pt sample is found to be three orders less compared to the reference Fe/Pt sample. The same order of THz amplitude was reported by Qiu *et al.* for C-plane α -Fe₂O₃/Pt [18]. The R-plane-oriented sample, on the other hand, shows one order of magnitude greater amplitude than A and C plane oriented α -Fe₂O₃/Pt. Our comparison confirms that the R-plane α -Fe₂O₃/Pt sample is more efficient for THz emission, even when compared with Qiu *et al.* [18].

APPENDIX D: THZ TIME-DOMAIN SPECTROSCOPY OF PURE α -Fe₂O₃ THIN FILMS

To verify the contribution of the substrate and the α -Fe₂O₃ thin films to the terahertz emission, we conducted THz measurements on R-, A-, and C-planes α -Fe₂O₃ thin films, as shown in Fig 9. We found no signal from the α -Fe₂O₃ thin films alone. This confirms that no significant terahertz signal is present from the ultrafast dipole radiation. The terahertz signal is known to be weaker in pure antiferromagnetic materials, as reported in previous studies [16,55].

-
- [1] V. Baltz, A. Manchon, M. Tsoi, T. Moriyama, T. Ono, and Y. Tserkovnyak, *Rev. Mod. Phys.* **90**, 015005 (2018).
- [2] T. Jungwirth, X. Marti, P. Wadley, and J. Wunderlich, *Nat. Nanotechnol.* **11**, 231 (2016).
- [3] J. Železný, P. Wadley, K. Olejník, A. Hoffmann, and H. Ohno, *Nat. Phys.* **14**, 220 (2018).
- [4] D. Xiong, Y. Jiang, K. Shi, A. Du, Y. Yao, Z. Guo, D. Zhu, K. Cao, S. Peng, W. Cai, D. Zhu, and W. Zhao, *Fundam. Res.* **2**, 522 (2022).
- [5] H. Bai, X. Zhou, Y. Zhou, X. Chen, Y. You, F. Pan, and C. Song, *J. Appl. Phys.* **128**, 210901 (2020).
- [6] J. R. Hortensius, D. Afanasiev, M. Matthiesen, R. Leenders, R. Citro, A. V. Kimel, R. V. Mikhaylovskiy, B. A. Ivanov, and A. D. Caviglia, *Nat. Phys.* **17**, 1001 (2021).
- [7] T. Kampfrath, M. Battiato, P. Maldonado, G. Eilers, J. Nötzold, S. Mährlein, V. Zbarsky, F. Freimuth, Y. Mokrousov, S. Blügel, M. Wolf, I. Radu, P. M. Oppeneer, and M. Münzenberg, *Nat. Nanotechnol.* **8**, 256 (2013).
- [8] T. Seifert, S. Jaiswal, U. Martens, J. Hannegan, L. Braun, P. Maldonado, F. Freimuth, A. Kronenberg, J. Henrizi, I. Radu, E. Beaupaire, Y. Mokrousov, P. M. Oppeneer, M. Jourdan, G. Jakob, D. Turchinovich, L. M. Hayden, M. Wolf, M. Münzenberg, M. Kläui *et al.*, *Nat. Photon.* **10**, 483 (2016).
- [9] T. J. Huisman and T. Rasing, *J. Phys. Soc. Jpn.* **86**, 011009 (2017).
- [10] Y. Wu, M. Elyasi, X. Qiu, M. Chen, Y. Liu, L. Ke, and H. Yang, *Adv. Mater.* **29**, 1603031 (2017).
- [11] Y. Ni, Z. Jin, B. Song, X. Zhou, H. Chen, C. Song, Y. Peng, C. Zhang, F. Pan, G. Ma, Y. Zhu, and S. Zhuang, *Rapid Res. Lett.* **15**, 2100290 (2021).
- [12] M. Chen, R. Mishra, Y. Wu, K. Lee, and H. Yang, *Adv. Opt. Mater.* **6**, 1800430 (2018).
- [13] G. Torosyan, S. Keller, L. Scheuer, R. Beigang, and E. T. Papaioannou, *Sci. Rep.* **8**, 1311 (2018).
- [14] R. Gupta, S. Husain, A. Kumar, R. Brucas, A. Rydberg, and P. Svedlindh, *Adv. Opt. Mater.* **9**, 2001987 (2021).
- [15] R. Schneider, M. Fix, J. Bensmann, S. Michaelis de Vasconcellos, M. Albrecht, and R. Bratschitsch, *Appl. Phys. Lett.* **120**, 042404 (2022).
- [16] H. Qiu, L. Zhou, C. Zhang, J. Wu, Y. Tian, S. Cheng, S. Mi, H. Zhao, Q. Zhang, D. Wu, B. Jin, J. Chen, and P. Wu, *Nat. Phys.* **17**, 388 (2021).
- [17] R. Agarwal, S. Kumar, N. Chowdhury, K. I. A. Khan, E. Yadav, S. Kumar, and P. K. Muduli, *Appl. Phys. Lett.* **122**, 082403 (2023).
- [18] H. Qiu, T. S. Seifert, L. Huang, Y. Zhou, Z. Kašpar, C. Zhang, J. Wu, K. Fan, Q. Zhang, D. Wu, T. Kampfrath, C. Song, B. Jin, J. Chen, and P. Wu, *Adv. Sci.* **10**, 2300512 (2023).
- [19] F. N. Kholid, D. Hamara, A. F. B. Hamdan, G. Nava Antonio, R. Bowen, D. Petit, R. Cowburn, R. V. Pisarev, D. Bossini, J. Barker, and C. Ciccarelli, *Nat. Commun.* **14**, 538 (2023).
- [20] L. Huang, Y. Zhou, H. Qiu, T. Guo, F. Pan, B. Jin, and C. Song, *Appl. Phys. Lett.* **119**, 212401 (2021).
- [21] K. Grishunin, E. A. Mashkovich, A. V. Kimel, A. M. Balbashov, and A. K. Zvezdin, *Phys. Rev. B* **104**, 024419 (2021).
- [22] P. R. Elliston and G. J. Troup, *J. Phys. C: Solid State Phys.* **1**, 169 (1968).
- [23] R. Lebrun, A. Ross, S. A. Bender, A. Qaiumzadeh, L. Baldrati, J. Cramer, A. Brataas, R. A. Duine, and M. Kläui, *Nature (London)* **561**, 222 (2018).
- [24] R. Lebrun, A. Ross, O. Gomonay, V. Baltz, U. Ebels, A. L. Barra, A. Qaiumzadeh, A. Brataas, J. Sinova, and M. Kläui, *Nat. Commun.* **11**, 6332 (2020).
- [25] I. Boverter, H. T. Simensen, A. Anane, M. Kläui, A. Brataas, and R. Lebrun, *Phys. Rev. Lett.* **126**, 187201 (2021).
- [26] H. Wang, Y. Xiao, M. Guo, E. Lee-Wong, G. Q. Yan, R. Cheng, and C. R. Du, *Phys. Rev. Lett.* **127**, 117202 (2021).
- [27] X. Huang, Y. Yang, and J. Ding, *Acta Mater.* **61**, 548 (2013).
- [28] Y. Cheng, S. Yu, M. Zhu, J. Hwang, and F. Yang, *Phys. Rev. Lett.* **124**, 027202 (2020).
- [29] A. Kozioł-Rachwał, N. Kwiatek, W. Skowroński, K. Grochot, J. Kanak, E. Madej, K. Freindl, J. Korecki, and N. Spiridis, *Phys. Rev. B* **106**, 104419 (2022).
- [30] D. A. Grave, D. Klotz, A. Kay, H. Dotan, B. Gupta, I. Visoly-Fisher, and A. Rothschild, *J. Phys. Chem. C* **120**, 28961 (2016).
- [31] P. Zhang, C.-T. Chou, H. Yun, B. C. McGoldrick, J. T. Hou, K. A. Mkhoyan, and L. Liu, *Phys. Rev. Lett.* **129**, 017203 (2022).
- [32] I. Yamaguchi, T. Manabe, T. Kumagai, W. Kondo, and S. Mizuta, *Thin Solid Films* **365**, 36 (2000).
- [33] S. Gota, M. Gautier-Soyer, and M. Sacchi, *Phys. Rev. B* **64**, 224407 (2001).
- [34] L. Cheng, X. Wang, W. Yang, J. Chai, M. Yang, M. Chen, Y. Wu, X. Chen, D. Chi, K. E. J. Goh, J.-X. Zhu, H. Sun, S. Wang, J. C. W. Song, M. Battiato, H. Yang, and E. E. M. Chia, *Nat. Phys.* **15**, 347 (2019).

- [35] J. Dho, C. W. Leung, Z. H. Barber, and M. G. Blamire, *J. Appl. Phys.* **97**, 10K101 (2005).
- [36] A. Serrano, J. Rubio-Zuazo, J. López-Sánchez, I. Arnay, E. Salas-Colera, and G. R. Castro, *J. Phys. Chem. C* **122**, 16042 (2018).
- [37] J. A. Moreno, M. A. Khan, Y. P. Ivanov, S. Lopatin, J. A. Holguín-Lerma, G. Marinaro, B. S. Ooi, H. Idriss, and J. Kosel, *ACS Appl. Energy Mater.* **2**, 8473 (2019).
- [38] A. M. Jubb and H. C. Allen, *ACS Appl. Mater. Interfaces* **2**, 2804 (2010).
- [39] A. Serrano, J. Fernandez, O. R. de la Fuente, and M. García, *Mater. Today Chem.* **4**, 64 (2017).
- [40] M. Kadleiková, J. Breza, and M. Veselý, *Microelectron. J.* **32**, 955 (2001).
- [41] E. Rongione, O. Gueckstock, M. Mattern, O. Gomonay, H. Meer, C. Schmitt, R. Ramos, T. Kikkawa, M. Mičica, E. Saitoh, J. Sinova, H. Jaffrès, J. Mangeney, S. T. B. Goennenwein, S. Geprägs, T. Kampfrath, M. Kläui, M. Bargheer, T. S. Seifert, S. Dhillon *et al.*, *Nat. Commun.* **14**, 1818 (2023).
- [42] P. Jiménez-Cavero, O. Gueckstock, L. Nádvořník, I. Lucas, T. S. Seifert, M. Wolf, R. Rouzegar, P. W. Brouwer, S. Becker, G. Jakob, M. Kläui, C. Guo, C. Wan, X. Han, Z. Jin, H. Zhao, D. Wu, L. Morellón, and T. Kampfrath, *Phys. Rev. B* **105**, 184408 (2022).
- [43] R. Rouzegar, L. Brandt, L. C. V. Nádvořník, D. A. Reiss, A. L. Chekhov, O. Gueckstock, C. In, M. Wolf, T. S. Seifert, P. W. Brouwer, G. Woltersdorf, and T. Kampfrath, *Phys. Rev. B* **106**, 144427 (2022).
- [44] A. Fognini, T. Michlmayr, A. Vaterlaus, and Y. Acremann, *J. Phys.: Condens. Matter* **29**, 214002 (2017).
- [45] C. Tzschaschel, K. Otani, R. Iida, T. Shimura, H. Ueda, S. Günther, M. Fiebig, and T. Satoh, *Phys. Rev. B* **95**, 174407 (2017).
- [46] X. Yang, T. Yu, C. Xu, J. Wang, W. Hu, Z. Xu, T. Wang, C. Zhang, Z. Ren, Z. A. Xu, M. Hirayama, R. Arita, and X. Lin, *Phys. Rev. B* **104**, 035157 (2021).
- [47] Y.-R. Shen, *The Principles of Nonlinear Optics* (Wiley-Interscience, New York, 1984).
- [48] T. Higuchi, N. Kanda, H. Tamaru, and M. Kuwata-Gonokami, *Phys. Rev. Lett.* **106**, 047401 (2011).
- [49] N. Kanda, T. Higuchi, H. Shimizu, K. Konishi, K. Yoshioka, and M. Kuwata-Gonokami, *Nat. Commun.* **2**, 362 (2011).
- [50] F. P. Chmiel, N. Waterfield Price, R. D. Johnson, A. D. Lamirand, J. Schad, G. van der Laan, D. T. Harris, J. Irwin, M. S. Rzechowski, C.-B. Eom, and P. G. Radaelli, *Nat. Mater.* **17**, 581 (2018).
- [51] P. Vaidya, S. A. Morley, J. van Tol, Y. Liu, R. Cheng, A. Brataas, D. Lederman, and E. Del Barco, *Science* **368**, 160 (2020).
- [52] J. Li, C. B. Wilson, R. Cheng, M. Lohmann, M. Kavand, W. Yuan, M. Aldosary, N. Agladze, P. Wei, M. S. Sherwin, and J. Shi, *Nature (London)* **578**, 70 (2020).
- [53] Y. Zhou, T. Guo, L. Han, L. Liao, W. He, C. Wan, C. Chen, Q. Wang, L. Qiao, H. Bai, W. Zhu, Y. Zhang, R. Chen, X. Han, F. Pan, and C. Song, *Sci. Adv.* **10**, eadk7935 (2024).
- [54] C. Sun, H. Yang, A. Brataas, and M. B. A. Jalil, *Phys. Rev. Appl.* **17**, 034028 (2022).
- [55] X. Zhou, B. Song, X. Chen, Y. You, S. Ruan, H. Bai, W. Zhang, G. Ma, J. Yao, F. Pan, Z. Jin, and C. Song, *Appl. Phys. Lett.* **115**, 182402 (2019).